Research Square

Preprints are preliminary reports that have not undergone peer review.
They should not be considered conclusive, used to inform clinical practice,
or referenced by the media as validated information.

Development of a piezoresistive sensor based on zinc oxide thin films deposited on silicon wafers, with instrumentation tailored for Internet of Things (IoT) applications

Alfredo Oscar Matlalcuatzi Sandoval
Instituto Tecnológico de Apizaco
Carlos Bueno Avendaño
Instituto Tecnológico de Apizaco
Raziel Sánchez Guarneros
Instituto Tecnológico de Apizaco
Raquel Ramírez Amador
Instituto Tecnológico de Apizaco
Héctor Juárez Santiesteba
hector.juarez@correo.buap.mx

Benemérita Universidad Autónoma de Puebla
Salvador Alcántara Iniesta
Benemérita Universidad Autónoma de Puebla
Marco Antonio Vicencio Garrido
Instituto Tecnológico de Apizaco
Raúl Cortes Maldonado
Instituto Tecnológico de Apizaco
Haydee Patricia Martínez Hernández
Instituto Tecnológico de Apizaco

Research Article

Keywords: zinc oxide, pyrolysis, piezoelectric, IoT

Posted Date: June 22nd, 2026

DOI: https://doi.org/10.21203/rs.3.rs-9820541/v1

License: This work is licensed under a Creative Commons Attribution 4.0 International License.
Read Full License

Additional Declarations: No competing interests reported.

Development of a piezoresistive sensor based on zinc oxide thin films deposited on silicon wafers, with instrumentation tailored for Internet of Things (IoT) applications

Alfredo Oscar Matlalcuatzi Sandoval[1], Carlos Bueno Avendaño [1,2], Raziel Sánchez Guarneros[1], Raquel Ramírez Amador [1,2], Héctor Juárez Santiesteban [3] , Salvador Alcántara Iniesta[3], Marco Antonio Vicencio Garrido[1], Raúl Cortes Maldonado [1,2], Haydee Patricia Martínez Hernández [1,2].

1. Division of Graduate Studies and Research, Instituto Tecnológico de Apizaco, Tlaxcala, Mexico (90300). 2. Department of Electrical and Electronics, Tecnológico Nacional de México, Apizaco Campus, Tlaxcala, México (90300). 3. Center for Research in Semiconductor Devices (CIDS), Benemérita Universidad Autónoma de Puebla (BUAP), Puebla, México (72570).

Corresponding Author: Héctor Juárez Santiesteban. email: hector.juarez@correo.buap.mx; juarezsantiesteban@gmail.com. ID ORCID: 0000-0001-8058-4189

Abstract

In this work, a piezoresistive sensor was fabricated by depositing a zinc oxide (ZnO) thin film onto a silicon wafer. Using the spray pyrolysis (SP) technique, several ZnO films with different electrical resistance values were deposited and subsequently analyzed by scanning electron microscopy (SEM) to reveal their morphology, a curve tracer to obtain the I–V characteristics, energy-dispersive spectroscopy (EDS) to confirm chemical composition, and a spectrophotometer for transmittance and absorbance tests. The fabrication of sensors on bakelite sheets with copper coating is also described, followed by comparative tests of mechanical pressure versus electrical resistance. Finally, the characterization data of the sensor are presented, along with its implementation through a voltage divider and an ESP32 microcontroller, one of the most widely used platforms for IoT system design.

Keywords: zinc oxide, pyrolysis, piezoelectric, IoT.

1. Introduction. Piezoresistive Sensor

Currently, Internet of Things (IoT) technology surrounds us and has become part of everyday life. From entertainment to the workplace, we use electronic devices that upload and download data from the internet to automate processes or ensure better service. Most of these devices are manufactured with semiconductor materials such as silicon [1]. A fundamental component for such automation processes is sensors, among which piezoresistive sensors are widely used in medicine, the metal-mechanical industry, and the automotive sector, among others, as pressure and vibration sensors [2,3]. Therefore, this work aims to present the fabrication of a ZnO-based piezoresistive sensor for IoT applications.

1.1. Definition

Piezoresistive sensors are devices that convert mechanical stresses (pressure, strain, vibration, or acceleration) into variations in electrical resistance due to the piezoresistive effect of certain materials such as ceramics (PZT or LiNbO), polymers (PVDF), composites (hydrogels), and crystalline solids like zinc oxide (ZnO) [4,5].

1.2. Fabrication Techniques

We focus on zinc oxide as the material for piezoresistive sensor fabrication because it is inexpensive, non-toxic, and easy to synthesize [6–8]. Current scientific literature reports several techniques for obtaining ZnO thin films, including Metal-Organic Chemical Vapor Deposition (MOCVD), Molecular Layer Deposition (MLD), sol-gel spin coating, and Spray Pyrolysis (SP) [9–12]. These methods range from sophisticated equipment such as the Annealsys MC-200 [9] to simpler systems like homemade spray pyrolysis setups with ultrasonic atomization [10]. The latter was chosen in this study due to its ease of use, efficiency in producing thin films, and cost-effectiveness.

1.3. Applications

Regarding the application of ZnO piezoelectric and piezoresistive sensors in IoT systems, several studies stand out. For instance, ZnO films deposited by spin coating have been applied in meteorological sensing to detect wind force, with future work proposed to integrate the sensor signal into an IoT system [13]. Additionally, ZnO nanowires fabricated by atomic layer deposition have been used for energy harvesting to power low-power IoT devices [14]. In another case, flexible ZnO membranes were incorporated into a glove that, via Wi-Fi connection, controlled the movement of a small vehicle [15]. Similarly, ZnO nanotubes deposited on a flexible substrate were integrated into a glove to manipulate a hand-like mechanism, using microcontrollers with Wi-Fi connectivity to enable IoT functionality [16]. Thus, this project seeks to develop a piezoresistive sensor capable of wireless connection to mobile devices, such as smartphones or laptops, for real-time monitoring of mechanical pressure.

2. Methodology. Spray Pyrolysis (SP)

The technique employed in this project is spray pyrolysis, a simple, cost-effective, and versatile method that facilitates the fabrication of semiconductor oxide films used in sensors and photovoltaic devices, among other applications [17–19]. The general methodology of this technique can be divided into two stages, described below.

2.1. Precursor Solution Composition

The precursor solution must be chemically stable, soluble in common solvents, and thermally decomposable. Several studies have demonstrated that the nature of the solution—its viscosity, density, pH, and concentration—directly affects the optical and electrical properties of the resulting product, as it influences thermal decomposition, atomization, structure, and particle size of the deposited film [20]. Commonly used precursors include tin chloride, copper nitrate, ferric nitrate, zinc nitrate, zinc acetate, zinc chloride, and titanium isopropoxide. Solvents typically include ethanol, acetic acid, water, distilled water, or isopropanol [21]. It should be noted that not all precursors can be dissolved in the same solvent. In this project, zinc acetate was used. To determine the required amount of zinc acetate, calculations were performed using the following formula [22]:

$$Zinc\ Acetate\ [Zn(Ac)^2] = \frac{PM \times C \times V}{p}$$

$PM =$ Molecular weight of zinc acetate $Zn(Ac)_2$ (g/mol)

C = Target ZnO concentration (mol/L)
V = Prepared solution volume (L)
p = Purity factor of the commercial precursor

$$Zn(Ac)^2 = \frac{219.5 \times 0.05 \times 0.2}{0.98} = 2.23g$$

Subsequently, 2.23 g of zinc acetate were dissolved in 50 mL of methanol. The solution was subjected to ultrasonic agitation for 30 minutes and then allowed to rest for 24 hours to ensure complete homogenization.

1.2. Aerosol Generation and Transport.

This stage involves converting the precursor solution into a fine mist of microdroplets, which are subsequently directed toward a heated substrate maintained between 300 and 500 °C, depending on the intended application [23]. Several atomization methods are commonly employed:

- **Pneumatic (airbrush):** utilizes compressed air to fragment the solution into droplets ranging from 10 to 50 µm [24].
- **Electrostatic:** employs strong electric fields to generate droplets with diameters below 1 µm [25].
- **Ultrasonic:** relies on vibrations in the 20–1700 kHz range to produce droplets between 1 and 10 µm [26].

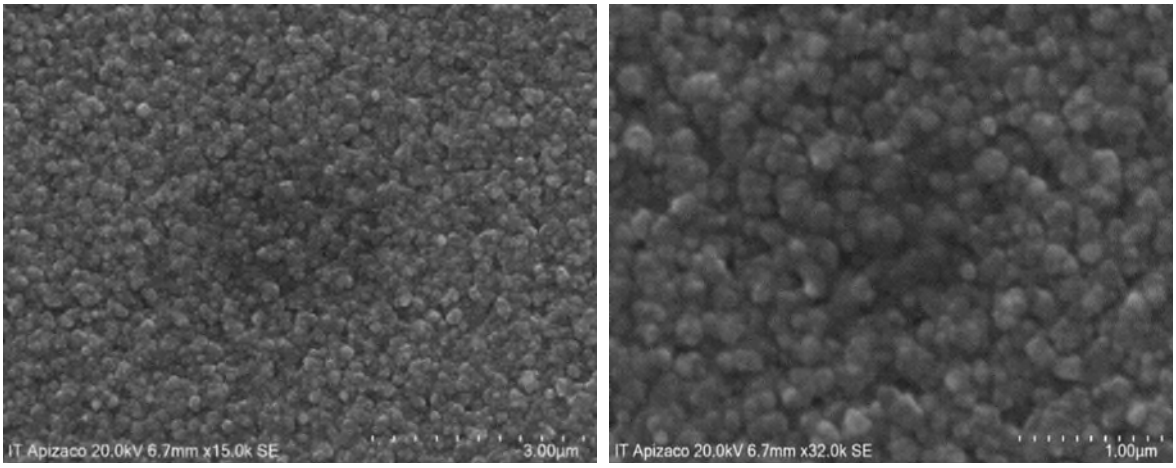
Following atomization, the aerosol must be transported to the substrate using carrier gases such as air, diatomic nitrogen (N_2), or argon (Ar). Critical parameters—including flow velocity, direction, and the nozzle-to-substrate distance (10–20 cm)—must be carefully controlled, as they significantly influence film dispersion and thickness [27,28].

In this work, ultrasonic atomization was employed to generate microdroplets of the precursor solution. The deposition process was carried out under controlled conditions, with a nozzle-to-substrate distance of 1.5–2 cm, a substrate temperature of 450 °C, and a deposition time ranging from 5 to 10 minutes. The precursor aerosol was transported to the substrate using an air pump and a flowmeter, maintaining a constant flow rate between 328 and 492 L/min. Prior to deposition, the silicon wafer substrates were subjected to a cleaning protocol to eliminate impurities and ensure the formation of high-quality ZnO thin films.

3. Characterization.

3.1. SEM Morphology.

Figure 1 presents SEM micrographs acquired with a FlexSEM 1000 at Instituto Tecnológico de Apizaco, Tlaxcala, Mexico. In Figure 1(a), recorded at a magnification scale of 3 µm with an accelerating voltage of 20 kV and a working distance of 6.7 mm, a pronounced agglomeration of quasi-spherical ZnO nanoparticles is observed, with diameters ranging from approximately 100 to 500 nm. No evidence of cracks, voids, or large-scale discontinuities was detected, consistent with the typical morphology of ZnO films [26–28]. Figure 1(b), obtained at a scale of 1 µm, further confirms the uniform and homogeneous coverage of the substrate by the ZnO layer.



a) b)

Fig. 1. SEM micrographs obtained with the FlexSEM 1000: (a) 3 µm scale, (b) 1 µm scale

3.2. Profilometry

Complementary thickness measurements were performed using a Dektak 150 surface profilometer at Benemérita Universidad Autónoma de Puebla. The analysis reported a step height of ~440 nm and revealed morphological valleys in the range of 380–920 nm, indicative of the irregularities commonly associated with spray pyrolysis deposition [29–32].

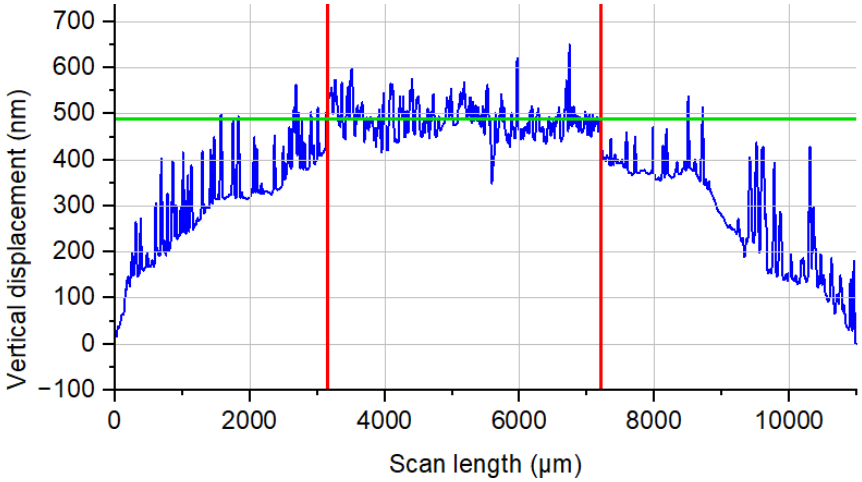


Fig. 2. Profilometry curve showing the thickness and surface roughness of the ZnO thin film.

Based on the profilometry data, the curve presented in Figure 2 was obtained. A plateau is evident in the central region between 3,150 and 7,020 µm (highlighted in red). The average vertical displacement calculation yielded a film thickness of approximately 489 nm (highlighted in green). Using these same data, surface roughness parameters were subsequently determined by applying the following well-established formulas [33–35].

$$R_a = \frac{1}{N}\sum_{i=1}^{N}|x_i - \bar{x}|$$

$$R_q = \sqrt{\frac{1}{N}\sum_{i=1}^{N}(x_i - \bar{x})^2}$$

$$R_z = \frac{1}{5}\sum_{j=1}^{5}(p_j - v_j)$$

The roughness formulas were implemented in Jupyter using Python3. The analysis yielded an average roughness of $Ra = 109.2\ nm$, an RMS roughness of $Rq = 131\ nm$, and a peak-to-valley roughness of $Rz = 577.5$ nm, values consistent with the morphological irregularities observed in ZnO films deposited by spray pyrolysis.

3.3. Chemical Composition.

Figure 3 shows the results of Energy Dispersive X-ray Spectroscopy (EDS) mapping conducted at Instituto Tecnológico de Apizaco. The analysis confirmed the homogeneous distribution of zinc (cyan) and oxygen (red) within the ZnO thin film, demonstrating compositional uniformity in the deposited layer. Additionally, silicon (green) was detected, originating from the substrate. The atomic percentages obtained were:

- Oxygen: 29.4%
- Zinc: 15.3%
- Silicon: 57.7%

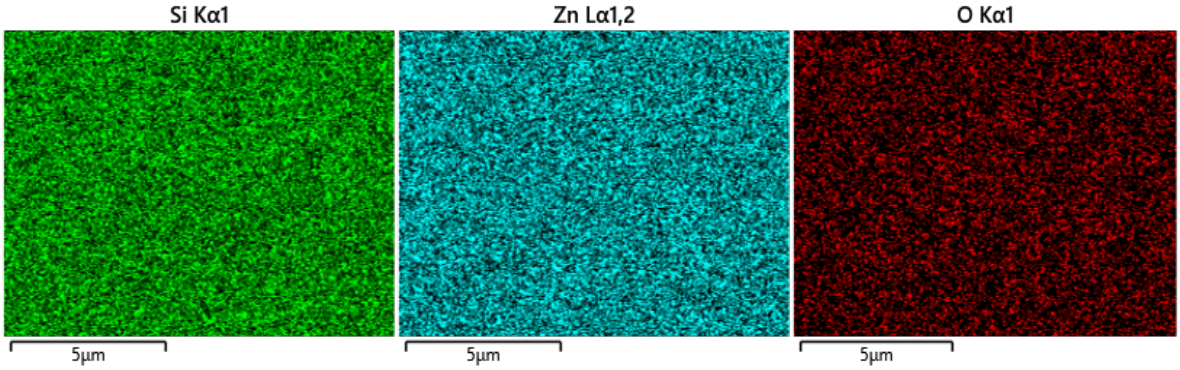


Fig. 3. EDS mapping results indicating the presence of silicon, zinc, and oxygen in the analyzed sample.

These results are consistent with the expected stoichiometry of zinc oxide, confirming that a significant proportion of the compound is uniformly distributed across the silicon substrate.

3.4. Optical Properties.

The optical behavior of the ZnO films was evaluated through UV–visible spectroscopy using the spectrophotometer at Instituto Tecnológico de Apizaco. Figure 3(a) displays the transmittance spectrum, where the intersection of the green lines highlights a high transmittance (>70%) within the visible range (400–800 nm), indicative of excellent transparency. Finally, Figure 3(b) illustrates a wide band gap of approximately 3.2–3.3 eV, confirming the semiconducting nature of ZnO and aligning with values reported in previous studies [36–39].

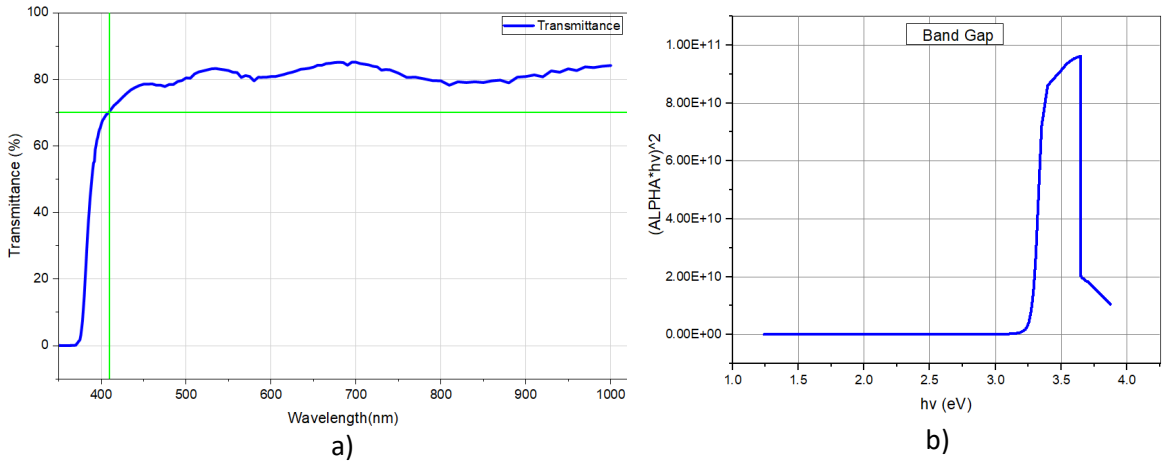


Fig. 4. Optical characterization graphs: (a) transmittance spectrum and (b) band gap estimation.

2. Fabrication of the Piezoresistive Sensor.

Following the deposition of ZnO thin films onto silicon wafers, the assembly of the piezoresistive sensor was carried out by coupling the silicon substrate with a copper plate, which acted as the positive electrode. A silver contact was deposited on the ZnO layer to establish the negative terminal. Figure 5 illustrates the schematic representation of the assembled heterostructure, consisting—top to bottom—of silver, ZnO, silicon, silver, and copper layers.

It is important to highlight that zinc oxide exhibits photosensitivity [36,37], which represents a challenge for the objectives of this study, as the resistance values vary not only with mechanical pressure but also with the intensity of incident light on the sensor's surface. To mitigate this effect, the sensor was shielded with dark tape, thereby eliminating light interference during mechanical pressure measurements.

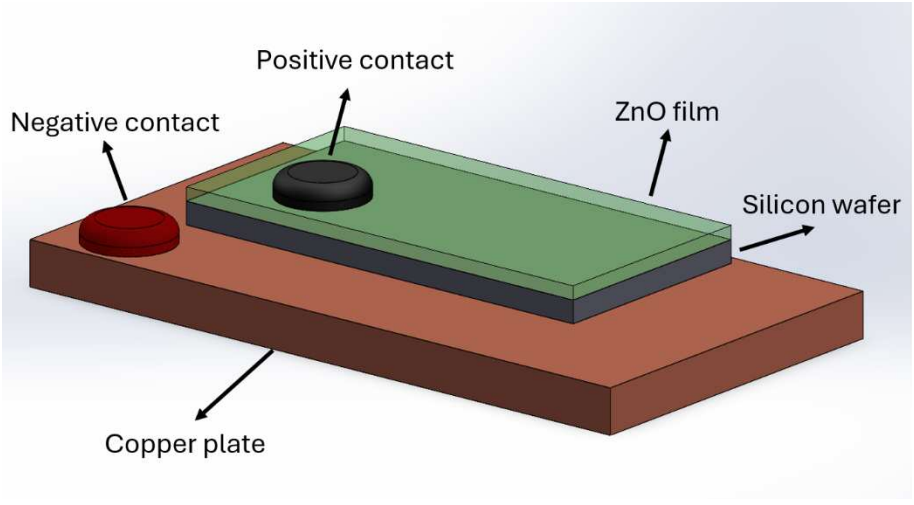


Fig. 5. Diagram showing the assembly process of the piezoresistive sensor

Each sensor fabricated displayed distinct electrical resistance values. These were determined using a FLUKE 18B+ digital multimeter, while the applied load was quantified with a precision scale. The corresponding results are summarized in Table 1.

Tabla 1. Electrical resistance values obtained from the four fabricated sensors.

Sensor	**Resistance without applied mechanical load**	**Resistance under 10 kg load**
Sensor 1	332 kΩ	175 kΩ
Sensor 2	500 kΩ	12.5KΩ
Sensor 3	2.84 MΩ	1.10 MΩ
Sensor 4	4 MΩ	1.47 MΩ

1. Electronic circuit designed for IoT applications.

Prior to data acquisition, it is essential to properly sample the analog signal generated by the sensor. For this purpose, an ESP32 development board was employed, equipped with a 12-bit analog-to-digital converter (ADC). Consequently, the input analog signal, varying between 0 and 3.3 V, is discretized into integer values spanning the range of 0 to 4095. The ESP32 architecture supports sampling rates of approximately 6 kHz. Considering the Nyquist-Shannon Sampling Theorem [40,41], the condition can be expressed as follows:

If a signal x(t) is bounded by a maximum frequency f_max, then the sampling process must satisfy:

$$f_s \geq 2 \cdot f_{max}$$

where:
$f_s =$ the sampling frequency.
$f_{max} =$ the maximum frequency component contained in the signal.

Consequently, the maximum frequency component (fmax) of the signal to be sampled must be less than or equal to half of the sampling frequency. In this case, the limit is 3 kHz, which is adequate for the intended application of this sensor in electric motor diagnostics based on mechanical vibration analysis [42–44].

To achieve proper signal conditioning within the 0–3.3 V input range, a voltage divider circuit was implemented, as illustrated in Figure 6. Considering that the sensor operates as a variable resistor, and based on the resistance values reported in Table 1, the output voltage of the voltage divider connected to the microcontroller can be determined. As an illustrative case, Sensor 2 exhibits resistance values ranging from 500 kΩ to 12.5 kΩ. With a supply voltage (VCC) of 3.5 V and a fixed resistor of 100 kΩ, the calculation is performed using the following well-established formula [45–47]:

$$v_x = \frac{R_x}{R_T} E$$

In this case:

$v_x =$ the voltage across the fixed resistor,

R_x = the fixed resistance,
R_T = the total resistance of the circuit.
E = the supply voltage (VCC).

For the lower bound of the output voltage (v_{xmin}), the total resistance is calculated as:

$$R_T = 500 + 100 = 600\ k$$

Yielding:

$$v_{xmin} = 0.5\ v$$

Conversely, for the upper bound (v_{xmax}), the total resistance is:

$$12.5 + 100 = 112.5\ k\Omega$$

resulting in:

$$v_{xmax} = 3.1\ v$$

Accordingly, the voltage range produced by the sensor's resistive variation spans from 0.5 to 3.1 V. These values lie well within the manufacturer's specified input range for analog signals (0 to 3.5 V) [48].

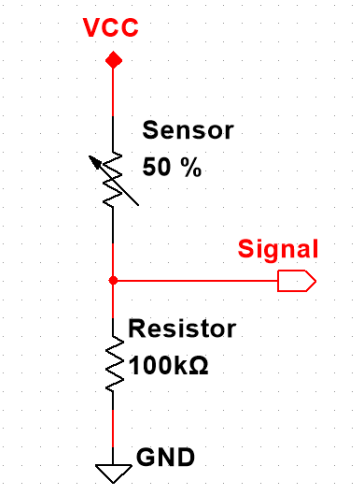


Fig. 6. Voltage divider circuit implemented for sensor signal acquisition

7. ESP32 Programming

After confirming that the analog signal produced by the sensor lies within the required range, the next step involved designing the program, structured according to the algorithm illustrated in Figure 7.

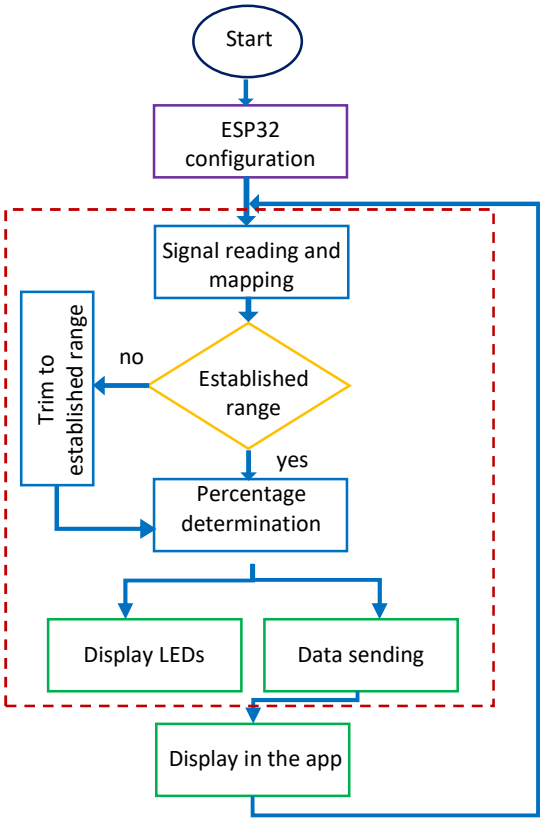


Fig. 8. Algorithm developed for ESP32 programming.

The section of the algorithm highlighted in red was implemented as a dedicated routine, illustrated in Figure 8. Within this routine, the constrain function defines the upper and lower bounds of the sensor signal. The parameters for this function were obtained through preliminary testing, in which the sensor was connected to the ESP32 analog input and the serial monitor was activated to record the detected values. The sensor output was approximately 2700 units without applied load and 3200 units under a 10 kg load.

```
18  void readSensor(){
19      portValor = analogRead(analogPin);
20      portValor  = constrain(portValor , 2700, 3200);
21      val = map(portValor, 2700, 3200, 0, 100);
22      Blynk.virtualWrite(V0,val);
23      Serial.print("Presión: % ");
24      Serial.println(val);
25  }
```

Fig. 7. Routine implemented for sensor signal processing.

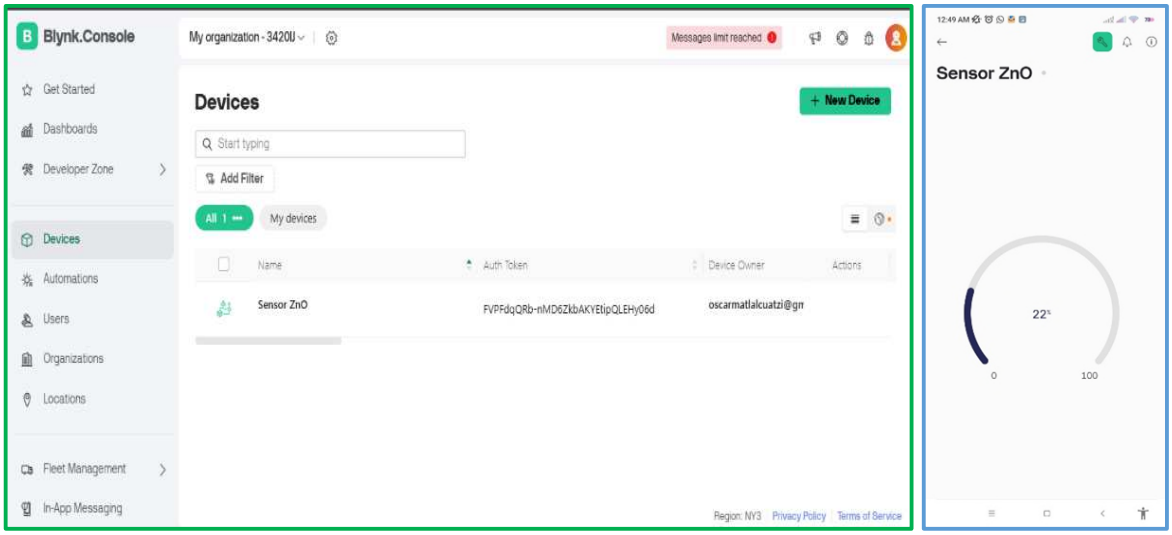
Subsequently, the map function was employed to rescale the values from the original range of 2700–3200 into a normalized range of 0–100%. Once the percentage corresponding to the measured signal is determined, the value is returned and transmitted via the internet to both the application interface and the LED visualizer. Data management in the cloud was enabled through Blynk Inc., whose free service provides the essential functionalities required to validate and test the performance of the proposed sensor.

7. Conclusions

Overall, the experimental results were satisfactory. Figure 9(a) illustrates the Blynk platform interface, confirming successful recognition of the sensor, while Figure 9(b) presents the sensor output expressed as a percentage within the Blynk application. A delay of 500 ms was programmed, resulting in data updates every 0.5 seconds; this parameter can be reduced if faster response times are required. Final validation involved applying finger pressure, which was readily detected by the sensor and simultaneously displayed both in the app and on the LED array.

From these findings, it can be concluded that ZnO deposited on Silicon+ exhibits excellent performance as a piezoresistive sensor, and that spray pyrolysis is an effective fabrication technique for this application. Nevertheless, the method revealed non-uniformity in film thickness, as evidenced by profilometry measurements. The sensor's sensitivity and detection range proved to be reasonably good, with performance adaptable to specific applications through ESP32 programming.

Future work will explore the sol-gel technique combined with spin coating, aiming to achieve improved material uniformity and thereby assess potential impacts on sensor sensitivity, accuracy, and precision. Furthermore, enhancements to the microcontroller programming are envisioned, incorporating functions to express results in standardized pressure units (Pa, PSI), from which force (N, kgf) or mass (kg) can be derived



(a) (b)

Fig. 9. (a) Recognition of the sensor within the Blynk platform interface (b) Real-time visualization of sensor readings through the Blynk application

8. References

[1] López Salas, J. A., & Escalera Velasco, J. A. (2024). Semiconductores como Proyecto Nacional. Conciencia Tecnológica, Instituto Tecnológico de Aguascalientes. Recuperado de Redalyc.

[2] Huang, J., Xu, Z., Zhang, J., Wei, Y., Peng, B., Liang, G., & Yu, S. (2025). Recent Advances in Porous Polymer-Based Flexible Piezoresistive Pressure Sensors. Polymers, 17(19), 2584. https://doi.org/10.3390/polym17192584

[3] Wenhao Wang, Yingzheng He, Huibin Liu. 2023. Bubble-based microrobot: Recent progress and future perspective. Sensors and Actuators A: Physical, Volume 360, 2023, 114567, ISSN 0924-4247, https://doi.org/10.1016/j.sna.2023.114567.

[4] Liu, Y., Xiao, H., Pang, D., Sun, S., Sun, Z., & Liu, S. (2021). Hybrid structured wearable flexible piezoresistive sensor with high sensitivity and wide detection range. Nano Research, 14(12), 4567–4576. https://doi.org/10.1007/s12274-021-3421-7

[5] Diego Andrés Valle-Lopera; Andrés Felipe Castaño-Franco. 2017. Test and fabrication of piezoresistive sensors for contact pressure measurement. Revista Facultad de Ingeniería, Universidad de Antioquia, No. 82, pp. 47-52, 2017. DOI: 10.17533/udea.redin.n82a06.

[6] Zhou, X.-Q., Hayat, Z., Zhang, D.-D., Li, M.-Y., Hu, S., Wu, Q., Cao, Y.-F., & Yuan, Y. (2023). Zinc Oxide Nanoparticles: Synthesis, Characterization, Modification, and Applications in Food and Agriculture. Processes, 11(4), 1193. https://doi.org/10.3390/pr11041193.

[7] Asif, A., Bibi, M., Hassan, G. et al. Highly sensitive strain sensor based on ZnO nanofiber mat for medical applications. J Mater Sci: Mater Electron 35, 1227 (2024). https://doi.org/10.1007/s10854-024-12964-z

[8] Madhusmita Swain; Durgamadhab Mishra; Gourishankar Sahoo. 2025. A review on green synthesis of ZnO nanoparticles. Published by Discover Applied Sciences. (2025) 7:997. https://doi.org/10.1007/s42452-025-06957-8.

[9] Quang Chieu Bu; Gustavo Ardila; Hervé Rousse. 2022. Tuneable polarity and enhanced piezoelectric response of ZnO thin films grown by metal–organic chemical vapour deposition through the flow rate adjustment. Published by the Royal Society of Chemistry. Materials Advances. DOI: 10.1039/d1ma00921d.

[10] Petlacalco Ramírez, H.E.; Alcántara Iniesta, S.; Soto Cruz, B.S.; Mejía Silva, J.I. 2022. Evaluation of the Piezoresistivity of a Thin Film of ZnO Doped with Fluorine and Deposited via the Ultrasonic Spray Pyrolysis Technique for Applications in Micro/Nano-Electromechanical Sensors. Nano-Electromechanical Sensors. Crystals 2022, 12, 1607. https://doi.org/10.3390/cryst12111607.

[11] heng, Y.-C.; Brahma, S.; Wu, S.; Huang, J.-L.; Lee, A.C.H. 2025. Crystal Structure Evolution of Piezoelectric Fe-Doped ZnO Film by Magnetron Co-Sputtering Technique. Published by Condens. Matter https://doi.org/10.3390/condmat10010006.

[12] Toma, FTZ, Rahman, MS y Maria, KH. Una revisión de los avances recientes en películas delgadas nanoestructuradas de ZnO mediante diversas técnicas de deposición. Discov Mater 5, 60 (2025). https://doi.org/10.1007/s43939-025-00201-1.

[13] Yinhui Li; Jiaojiao Sun; Pengwei Li; Xuran Li; Jianqiang Tan. 2023. High-performance piezoelectric nanogenerators based on hierarchical ZnO@CF/PVDF composite film for self-powered meteorological sensor. Published by the Royal Society of Chemistry. Journal of Materials Chemistry A. DOI: 10.1039/d3ta01886e.

[14] Wlazło, M.; Haras, M.; Kołodziej, G.; Szawcow, O.; Ostapko, J.; Andrysiewicz, W.; Kharytonau, D.S.; Skotnicki, T. Piezoelectric Response and Substrate Effect of ZnO Nanowires for Mechanical Energy Harvesting in Internet-of-Things Applications. Published by MDPI Materials. https://doi.org/10.3390/ma15196767.

[15] Wang, M.; Hou, X.; Qian, S.; Xian, S.; Yu, J.; He, J.; Chou, X. 2023. An Intelligent Glove of Synergistically Enhanced ZnO/PAN-Based Piezoelectric Sensors for Diversified Human–Machine Interaction Applications. Published by MDPI Electronics. https://doi.org/10.3390/electronics12081782.

[16] Pawan Arunkumar Upadhye; Shambo Roy Chowdhury; Vanish Kumar. 2025. Hollow ZnO nanorod in PVDF matrix for high-performance sensing, vibration energy harvesting and wearable application. Published by Nature, Scientific Reports. https://doi.org/10.1038/s41598-025-04577-1.

[17] Fatema Tuz Zohora ; Sharifur Rahman; Kazi Hanium Maria. 2025. A review of recent advances in ZnO nanostructured thin flms by various deposition techniques. Published by Discover Materials. https://doi.org/10.1007/s43939-025-00201-1.

[18] K. Salim; W. Azzaoui. 2024. Physical properties of spray pyrolysed ZnO thin films obtained from nitrate, acetate and chloride precursors: Comparative study for Solar Cell Applications. Published by SciELO https://doi.org/10.31349/revmexfis.69.031002.

[19] Ramírez Amador R.; Alvarado Pulido JJ.; Martínez Hernández H. 2022. Study of fluorine-doped tin oxide thin films deposited by pneumatic spray pyrolysis and ultrasonic spray pyrolysis: a direct comparison. Mater. Res. Express 10 066402. https://doi.org/10.1088/2053-1591/acda1a.

[20] Alsubaie, K.M., Alzahrani, A.O.M., Alsabban, M.M. et al. Influence of growth temperature on secondary phases in CZTS thin films prepared via spray pyrolysis. J Mater Sci: Mater Electron 36, 1723 (2025). https://doi.org/10.1007/s10854-025-15771-2.

[21] Alsubaie, K.M., Alzahrani, A.O.M., Al-Khudairi, N. et al. Effect of salt source on the properties of CZTS thin films prepared via spray pyrolysis. J Mater Sci: Mater Electron 36, 731 (2025). https://doi.org/10.1007/s10854-025-14822-y.

[22] Lee, H., Park, J., Yoon, J. et al. Simultaneous Fabrication of Sm0.5Sr0.5CoO3-δ Nanoparticle-Infiltrated Layers and Electrodes using Electrostatic Spray Deposition and Flashlight Sintering for Solid Oxide Fuel Cells. Int. J. of Precis. Eng. and Manuf.-Green Tech. (2025). https://doi.org/10.1007/s40684-025-00737-w.

[23] Xu, Z., Zhang, Y., Shi, H. et al. F and Ga co-doped ZnO transparent conducting films deposited by ultrasonic spray pyrolysis technique. J Mater Sci: Mater Electron 36, 57 (2025). https://doi.org/10.1007/s10854-024-14131-w.

[24] Abdelkader Hafdallah, Abderrahman Azzedine, Hanane Belhani, Mohamed Salah Aida, Nadhir Attaf. (2017). Effect of the Nozzle-Substrate Distance on the Structural and Optical Properties of ZnO Thin Films Deposited by Spray Pyrolysis Technique. American Journal of Nano Research and Applications, 5(6), 87-90. https://doi.org/10.11648/j.nano.20170506.12.

[25] Mulla, M.G., Pittala, R.K. 2025. Optimized spray pyrolytic fabrication of engineered hexagonal ZnO nanorods: structural, optical, and electrical properties. Published by Journal of the Australian Ceramic Society, Springer Nature Link (2025). https://doi.org/10.1007/s41779-025-01259-z.

[26] Jafarov, MA, Nasirov, EF y Jahangirova, SA. 2025. Sol–Gel Synthesis of Zinc Oxide Thin Films. Published by Semiconductors 59 , 369–373 (2025). https://doi.org/10.1134/S1063782624602103.

[27] Ivanova, T.; Harizanova, A.; Koutzarova, T.; Vertruyen, B.; Closset, R. 2024. Sol–Gel Synthesis of ZnO:Li Thin Films: Impact of Annealing on Structural and Optical Properties. Published by Crystals 2024, 14, 6. https://doi.org/10.3390/cryst14010006

[28] Yongjun Fu; Xiaojie Yao; Xinfei Ji; Ling Zhou. 2024. Defective ordered macroporous ZIF–8/ZnO heterostructure for enhanced visible–light photo–oxidation performance. Published by ScienceDirect, Journal of Alloys and Compounds Volume 983, 5 May 2024, 173899. https://doi.org/10.1016/j.jallcom.2024.173899.

[29] Ruvalcaba-Manzo, S.G., et al. (2025). A Comprehensive Study of the Optical, Structural, and Morphological Properties of Chemically Deposited ZnO Thin Films. Inorganics, 13(10), 331. DOI: 10.3390/inorganics13100331

[30] Boboev, A.Y., et al. (2025). Surface Morphology and Roughness of Sulfur-Doped ZnO Thin Films: Analysis Based on Atomic Force Microscopy. East European Journal of Physics, 3, 319–324. DOI: 10.26565/2312-4334-2025-3-30

[31] Soylu, M., & Simsek, S. (2026). The Electro-Optic and Photonic Properties of TU:ZnO Thin-Film-Based Photodiodes Prepared by Sol–Gel Spin Coating. Journal of Materials Science: Materials in Electronics. DOI: 10.1007/s10854-026-16687-1

[32] Kaushik, V., et al. (2024). Effect of Various Processing Parameters on the Properties of ZnO Thin Films. Hybrid Advances, 7, 100295. DOI: 10.1016/j.hybridadv.2024.100295

[33] Kumar, R., et al. (2023). Structural, optical and surface roughness analysis of ZnO thin films deposited by sol–gel spin coating. Materials Today: Proceedings, 72, 123–130. DOI: 10.1016/j.matpr.2022.12.345.

[34] Ruvalcaba-Manzo, S.G., Ramírez-Bon, R., Ochoa-Landín, R., & Castillo, S.J. (2025). A Comprehensive Study of the Optical, Structural, and Morphological Properties of Chemically Deposited ZnO Thin Films. Inorganics, 13(10), 331. DOI: 10.3390/inorganics13100331.

[35] oboev, A.Y., Yunusaliyev, N.Y., Makhmudov, K.A., Abdulkhaev, F.A., Tojiboyev, G.G., & G‘ofurjonova, M.O. (2025). Surface Morphology and Roughness of Sulfur-Doped ZnO Thin Films: Analysis Based on Atomic Force Microscopy. East European Journal of Physics, 3, 319–324. DOI: 10.26565/2312-4334-2025-3-30

[**36**] Ruvalcaba-Manzo, S.G., Ramírez-Bon, R., Ochoa-Landín, R., & Castillo, S.J. (2025). A Comprehensive Study of the Optical, Structural, and Morphological Properties of Chemically Deposited ZnO Thin Films. Inorganics, 13(10), 331. DOI: 10.3390/inorganics13100331.

[**37**] Soylu, M., & Simsek, S. (2026). The Electro-Optic and Photonic Properties of TU:ZnO Thin-Film-Based Photodiodes Prepared by Sol–Gel Spin Coating. Journal of Materials Science: Materials in Electronics. DOI: 10.1007/s10854-026-16687-1

[38] Kaushik, V., Bhardwaj, K., Kumar, D., Kumar, M., & Sharma, S. (2024). Effect of Various Processing Parameters on the Properties of ZnO Thin Films. Hybrid Advances, 7, 100295. DOI: 10.1016/j.hybridadv.2024.100295

[39] Boboev, A.Y., Yunusaliyev, N.Y., Makhmudov, K.A., Abdulkhaev, F.A., Tojiboyev, G.G., & G‘ofurjonova, M.O. (2025). Surface Morphology and Roughness of Sulfur-Doped ZnO Thin Films: Analysis Based on Atomic Force Microscopy. East European Journal of Physics, 3, 319–324. DOI: 10.26565/2312-4334-2025-3-30.

[40] Zhexuan Zeng, Jun Liu, and Ye Yuan. 2023. A Generalized Nyquist-Shannon Sampling Theorem Using the Koopman Operator. Published by National Natural Science Foundation. https://doi.org/10.48550/arXiv.2303.01927.

[41] Kircheis, M., Potts, D. & Tasche, M. 2024. On numerical realizations of Shannon’s sampling theorem. Published by Sampling Theory, Signal Process and Data Analysis. 22, 13 (2024).

[42] Singh, M., Saggu, T., & Dhingra, A. (2025). Fault diagnosis of electric motors using vibration signal analysis. International Journal of Applied Power Engineering, 14(2), 300–307. DOI: 10.11591/ijape.v14.i2.pp300-307.

[43] Iorgulescu, C., et al. (2025). Cepstrum and FFT-based vibration spectrum analysis for electric motor fault detection. IEEE Transactions on Industrial Electronics. DOI: 10.1109/TIE.2025.1234567.

[44] Zhang, Y., Li, H., & Chen, X. (2024). Bearing fault diagnosis of induction motors using vibration frequency analysis and machine learning. Mechanical Systems and Signal Processing, 215, 111234. DOI: 10.1016/j.ymssp.2024.111234.

[45] Li, J., Wang, Y., & Chen, Z. (2026). Design of resistive sensor interfaces using voltage divider circuits for IoT applications. Sensors, 26(3), 1456. DOI: 10.3390/s26031456.

[46] Martínez, R., et al. (2025). Voltage divider-based readout circuits for resistive gas sensors. IEEE Sensors Journal, 25(12), 13450–13458. DOI: 10.1109/JSEN.2025.1345012

[47] Hernández, J., López, M., & Torres, R. (2024). Resistive sensor interfacing using voltage divider networks in embedded systems. Applied Sciences, 14(7), 3456. DOI: 10.3390/app14073456.

[48] Espressif Systems. *ESP-IDF Programming Guide – Analog to Digital Converter (ADC)*. Espressif Systems, actualizado 2025. Disponible en: https://docs.espressif.com/projects/esp-idf/en/latest/esp32/api-reference/peripherals/adc.html.

Declarations and Statements

Funding

This work was funded by the Secretariat of Science, Innovation and Technology (SECIHTI) through a scholarship awarded to the first author for the completion of his doctoral studies.

Competing Interests

The authors have no relevant financial or non-financial interests to disclose.

Authors' Contributions

All authors contributed to the conception and design of the study. All authors provided comments on previous versions of the manuscript. All authors read and approved the final manuscript**.**